scientific reports

Check for updates

OPEN

Mechanisms of global climate change during the five major mass extinctions

Kunio Kaiho

Since the emergence of diverse animal phyla around 500 million years ago, five major mass extinction events have occurred, each coinciding with abnormal climate changes. We analyzed sedimentary organic molecules from the first and least understood extinction event at the end of the Ordovician period. We divided all five major extinctions into two phases each, totaling ten events, and examined the relationship between climate shifts and the "coronene index"—an indicator of heating temperatures in sedimentary rocks caused by volcanic activity or meteorite impacts. As a result, we found that four of the five extinctions began with global cooling and ended with warming, while one started with an unknown anomaly and also ended with warming. During the initial extinction phases, two events showed low-temperature heating, two high-temperature, and one moderate-temperature. All subsequent warming phases showed moderate-temperature heating. These findings suggest that large-scale volcanic eruptions and meteorite impacts heated sulfides, sulfates, and hydrocarbons at varying temperatures, releasing SO_2 or soot into the stratosphere, blocking sunlight, and triggering global cooling and extinction. This was followed by moderate heating of hydrocarbons and carbonates, increasing CO_2 emissions and driving long-term global warming, leading to secondary extinction events.

Marine animal diversity at the genus level declined rapidly during five major mass extinction events in the Phanerozoic Eon[1,2]. The last three of these events also significantly affected terrestrial tetrapods[3]. Extensive research has examined the relationship between these mass extinctions and climate change[4–9]. While volcanic activity is considered the primary driver of most extinctions, the Cretaceous-Paleogene (K-Pg) extinction is widely attributed to an asteroid impact[10–12]. Global warming played a dominant role in the end-Permian (end-P) extinction, whereas cooling followed by warming characterized the Late Ordovician (LO), Late Devonian Frasnian-Famennian (F-F) boundary, end-Triassic (end-T), and K-Pg extinctions[4–9,13] (Table 1).

The coronene index serves as a proxy for the heating temperature of sedimentary organic matter and is derived from the ratio of the 7-ring polycyclic aromatic hydrocarbon (PAH) coronene to the sum of 5-, 6-, and 7-ring PAHs, including benzo(e)pyrene, benzo(ghi)perylene, and coronene[12,14–17]. Coronene requires significantly higher formation temperatures than smaller PAHs[18]. Kaiho (2024)[12] demonstrated a strong correlation between global surface temperature anomalies and coronene index values, linking them to heating events associated with volcanic eruptions and asteroid impacts.

Under normal conditions, the coronene index remains around 0.1[14–16,19]. Diagenetic processes do not significantly generate coronene due to its low abundance, and Proterozoic-Paleozoic strata are dominated by smaller PAHs[14,15,20]. Wildfires, particularly those in grasslands, burn at relatively low temperatures and do not produce significant amounts of coronene. Marine sediment samples containing wildfire-derived PAHs consistently exhibit low coronene index values, challenging the idea that coronene enrichment results solely from wildfires. Volcanic activity, particularly plume volcanism, can generate coronene due to higher mantle temperatures, resulting in medium coronene index values. In contrast, large-scale continental rift volcanism produces low coronene index values[16].

The coronene index distinguishes geological events based on heating intensity. Asteroid impacts and high-temperature plume volcanism result in coronene index values ranging from 0.7 to 1.0, while large plume volcanism produces values between 0.2 and 0.7. Background conditions and other volcanic activity yield values between 0 and 0.2[12,16]. Laboratory experiments indicate that different heating processes have distinct climatic effects. Low-temperature sulfide heating or high-temperature sulfate heating primarily releases sulfur dioxide (SO_2), driving global cooling. Intermediate-temperature heating of hydrocarbons and carbonates primarily

Department of Earth Science, Graduate School of Science, Tohoku University, Sendai 980- 8578, Japan. email: kunio.kaiho.a6@tohoku.ac.jp

Mass extinction	Event	Biozone or event	Duration between two events (m.y.)	Climate change	Hg/TOC anomaly	Coronene index
KPgME	deep-water	P0	0.1	Warming	high	medium
	main	*A. mayaroensis*/P0		Cooling	spike	high
ETME	Event 3	Recovery in end T	0.2	Warming	spike	medium
	Events 1–2	initial CIE & ETE		Cooling	spike	Low to medium
PTME	eTE	*H. parvus*	0.06	Warming	high	medium
	EPE	Top of *C. yini*		?	spike	medium
FFME	minor	mid-*triangularis*	0.3	Warming	No	medium
	main	Top of *linguiformis*		Cooling	spike	high
LOME	Pulse 2	lower *persculptus*	0.5	Warming	spike	medium
	Pulse 1	Top of *pacificus*		Cooling	spike	low

Table 1. Double events in each major mass extinction: timing and characteristics. See also Table S1 for detail.

emits carbon dioxide (CO_2), leading to global warming. Medium- to high-temperature shock heating from meteorite impacts generates soot and sulfur trioxide (SO_3), further contributing to global cooling[12,16].

Kaiho (2024)[12] concluded that mass extinctions were triggered by sedimentary rock heating in Large Igneous Provinces (LIPs) and by high-temperature heating of impact target rocks, such as those at the Chicxulub impact site. Low-temperature heating released SO_2 from sulfides without significant CO_2 emissions, leading to global cooling. Intermediate-temperature heating of hydrocarbons and carbonates released substantial CO_2, contributing to global warming. High-temperature sulfate heating resulted in massive SO_2 emissions, also driving global cooling.

Despite these findings, coronene index data are missing for key extinction phases, particularly the Late Ordovician Mass Extinction (LOME) and delayed extinction events that followed the primary extinction phases in all five major mass extinctions. This study aims to address these gaps by identifying two distinct extinction events within each of the five major mass extinctions and analyzing coronene index values for ten extinction phases, encompassing both primary and delayed events. To accomplish this, I conducted a new PAH analysis of the first and second LOME using sediment samples from the Wangjiawan site, located on the outer shelf of the South China Craton during the Ordovician–Silurian transition (see Methods for details). I then reviewed temperature anomalies from the literature to further investigate the role of heating temperatures in driving climate change during these mass extinction events.

Results

Identification of two events in each mass extinction event

Each of the five major mass extinctions consisted of two distinct extinction pulses. The LOME experienced two pulses of biodiversity loss[4,21,22]. The Frasnian-Famennian Mass Extinction (FFME) was followed by a minor biotic decline near the top of the mid-*triangularis* zone of conodonts[6] (Table 1). The End-Permian Extinction (EPE) was accompanied by a second extinction pulse in the earliest Triassic (eTE) within the Permian-Triassic mass extinction (PTME)[23]. The End-Triassic Mass Extinction (ETME) consisted of primary extinction pulse (Events 1 and 2), followed by Event 3 characterized by low biodiversity (Event 3)[16,24]. The Cretaceous-Paleogene Mass Extinction (KPgME) initially affected surface marine organisms, followed by a minor delayed extinction event among deep-water species in the P0 zone of planktonic foraminifera[19] (Table 1). The time intervals between these paired extinction events are estimated to be 0.5, 0.3, 0.06, 0.2, and ~0.1 million years for LOME, FFME, PTME, ETME, and KPgME, respectively, based on the time scales of Gradstein et al.[25] and Burgess et al.[26] (Table 1).

Surface temperature anomaly

The primary (first) marine extinction events correspond to cooling episodes, except for the end-Permian extinction. The recorded global surface temperature anomalies for these events are −10, −8, 0, −8, and −10 °C, respectively[12,27] (Table S1, Fig. 1). These values are based on conodont $\delta^{18}O_{PO4}$ data for the LOME[4], Frasnian-Famennian (F-F) extinction[5,6], and EPE (EPE-eTE)[7] (Chen et al., 2016); oyster $\delta^{18}O_{carb}$ data for the ETE[8]; and TEX_{86} organic paleothermometry for the Cretaceous-Paleogene (K-Pg) extinction[9,28].

In contrast, the delayed marine extinction events correspond to warming episodes. The associated global surface temperature anomalies for these events are +10, +7, +14, +11, and +7 °C, respectively[4–9] (Table S1, Fig. 1).

Coronene index and climate change

I obtained the coronene index from two LOME events at Wangjiawan (Fig. 2; Table 2, see Methods). I also utilized published coronene index data from eight biotic crises, representing two extinction events in each of the other four major mass extinctions. The data were plotted in a cross-plot diagram, correlating the coronene index with global surface temperature anomalies (Fig. 1, Table S1). These cross-plots categorize the ten events from the five major mass extinctions into four distinct groups: (i) low coronene index values (0–0.2) associated with global cooling, (ii) medium values (0.2–0.8) linked to global warming, (iii) high values (0.8–1.0) with global cooling, and (iv) medium values indicating a sill-magma heating implying global cooling followed by warming, but no record of cooling, which may have been due to short-term < 100 years SO_2 degassing.

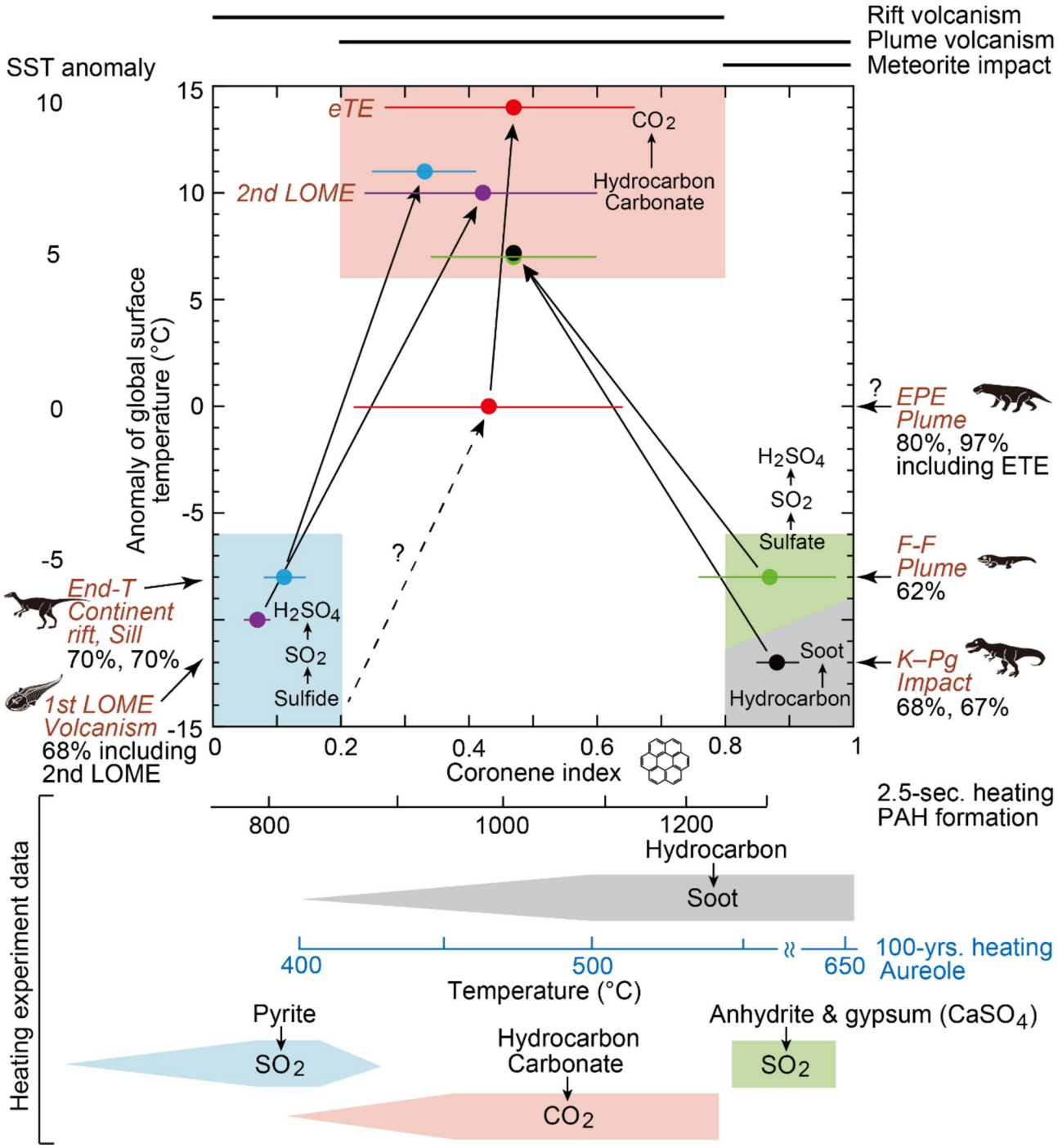

Fig. 1. Cross plots of the coronene index versus global surface temperature anomalies for 10 biotic crises during the five major mass extinctions. These plots also include heating temperatures derived from experimental data and the major emission gases/particles influencing climate change[12]. Event names are followed by their causes and species extinction percentages in marine and terrestrial environments[27]. Black long arrows in the upper figure frame indicate directional changes. Global surface temperature anomalies are calculated from references[4–9,28]. Heating experimental data after Norinaga et al.[18], Kaiho et al.[16], and Kaiho[12]. The relationship between the two temperature scales, which connects the upper and lower figures, is based on the Arrhenius equation. For further details, see Kaiho (2024)[12] and Table S1. Horizontal bars indicate ± SD. The SST anomaly records for the five major mass extinctions have been converted to global surface temperature anomalies[27] (see methods of Kaiho[27].

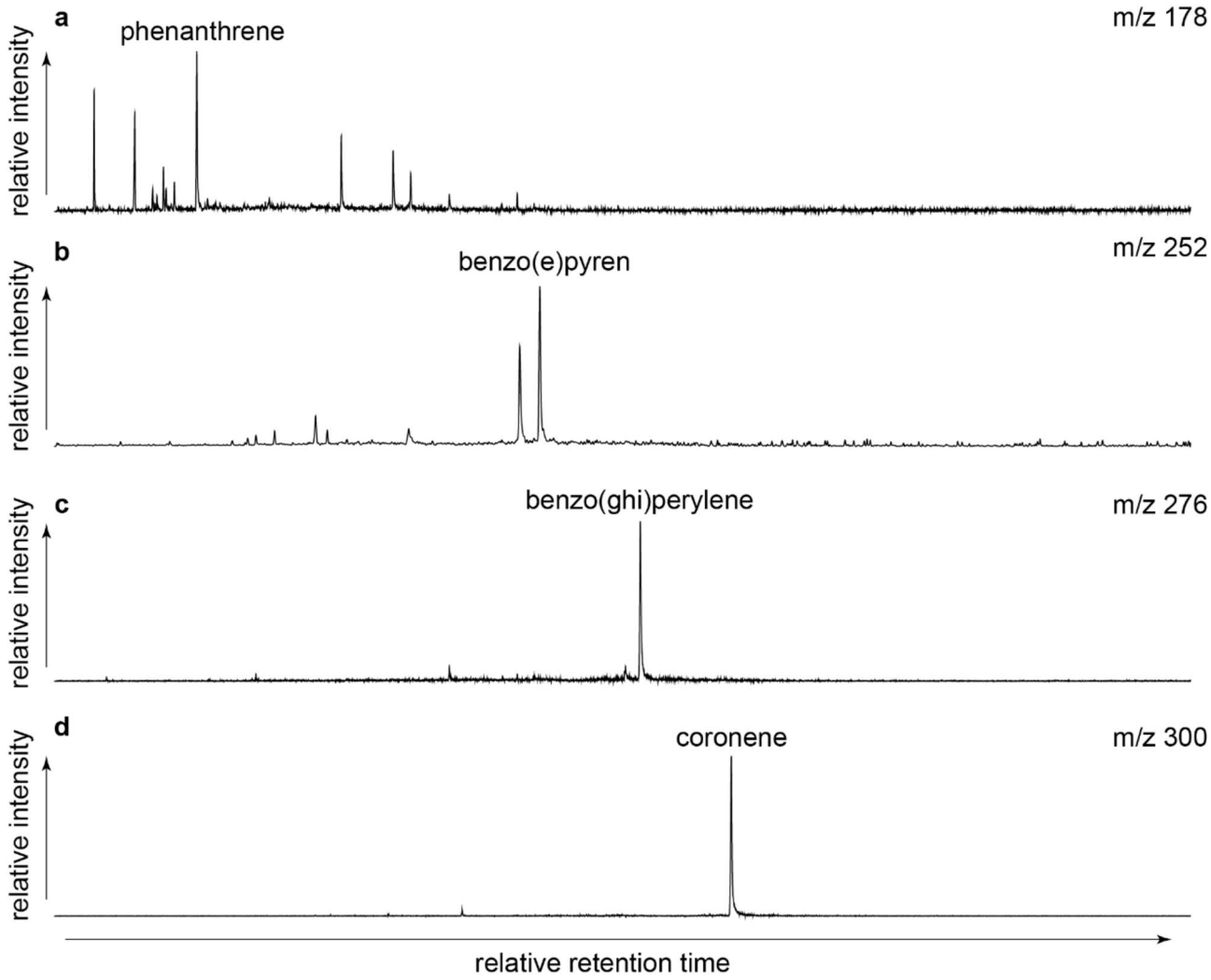

Fig. 2. Gas chromatogram of polycyclic aromatic hydrocarbons (PAHs) from sample CHWJ 2.39–2.42, collected from the Wanjiawan River section, South China. The sample corresponds to LOME Pulse 2. Major PAH peaks are labeled: (**a**) phenanthrene, (**b**) benzo(e)pyren, (**c**) benzo(ghi)perylene, and (**d**) coronene.

The background coronene index value across the five major mass extinction intervals is 0.09 ± 0.07 (mean ± standard deviation, $n = 48$) (Table S1). In contrast, coronene index values during the primary (first) marine extinction events for each of these five major extinctions are as follows: 0.07 ± 0.02 ($n = 3$) for the LOME Pulse 1, 0.87 ± 0.11 ($n = 15$) for the Frasnian-Famennian (F-F), 0.44 ± 0.22 ($n = 12$) for the PTME EPE, 0.11 ± 0.03 ($n = 30$) for the ETE Event 1, and 0.88 ± 0.03 ($n = 11$) for the KPg main (Tables 2 and S1, Fig. 1).

Of these values, 0.07 at LOME pulse 1 and 0.11 at ETE event 1 are similar to the background values, as well as to those of their respective periods, 0.04 ± 0.00 ($n = 2$) and 0.13 ± 0.04 ($n = 13$) (Table S1). However, the EGC index—calculated as (e + g + c)/p, where *e* is benzo(e)pyrene, *g* is benzo(ghi)perylene, *c* is coronene, and *p* is phenanthrene—at LOME Pulse 1 and ETE Event 1 is enriched relative to background values by factors of 2.7 and 8.7, respectively, as shown by the enrichment factors (EF) in Table S1. A t-test on the EGC index between the primary event and background values yields P values of 0.021 and 0.030, respectively. These statistically significant differences indicate that higher heating temperatures, compared to background conditions, occurred at both LOME pulse 1 and ETE Event 1, consistent with the elevated formation temperatures required for coronene, benzo(ghi)perylene, and benzo(e)pyrene relative to phenanthrene[18].

The coronene index values during the delayed marine extinction events or periods of low diversity associated with each of the five major extinctions are as follows: 0.42 ± 0.19 ($n = 2$) for the LOME Pulse 2, 0.47 ± 0.14 ($n = 6$) for the FFME minor, 0.47 ± 0.20 ($n = 5$) for the eTE, 0.33 ± 0.08 ($n = 4$) for the ETE Event 3, and 0.47 ± 0.00 ($n = 2$) for the KPgME deep-water event. All of these values fall within the medium range (0.2–0.8), suggesting moderate heating temperatures of sedimentary organic matter (Fig. 1). The PAH chromatogram for LOME Pulse 2 is shown in Fig. 2.

The delayed extinction event values are statistically differentiated from the primary extinction event values, as indicated by t-test P values of 0.043 for LOME, 1.1×10^{-6} for FFME, 4.8×10^{-16} for ETME, and 1.5×10^{-9} for KPgME. In contrast, the coronene index values for the End-Permian Extinction (EPE) and earliest-Triassic

Event	Sample CHWJ	Height (m)	Lithology	Coronene index	EGC index	EGC $index_{EF}$	TOC (%)	Fossil zone or carbon isotope event	SST anomaly (°C)
	2.55–2.58	2.565	Limestone	0.02	0.6	1.02	6.98	*persculptus*	
LOME Pulse 2	2.39–2.42	2.405	Limestone	0.6	7.4	12.54	0.11	*extraordinarius*	+7
LOME Pulse 2	2.33–2.36	2.345	Limestone	0.23	4.1	6.95	0.62	*extraordinarius*	+7
	2.03–2.06	2.045	Calcareous shale	0.05	1.28	2.17	4.14	*extraordinarius*	
	1.98–2.03	2.005	Calcareous shale	0.1	1.69	2.86	6.22	*extraordinarius*	
	1.89–1.97 up	1.95	Calcareous shale	0.1	1.69	2.86	5.32	*extraordinarius*	
LOME Pulse 1	1.89–1.97 low	1.91	Calcareous shale	0.05	1.36	2.31	4.98	*pacificus*	−7
LOME Pulse 1	1.86–1.89	1.875	Calcareous shale	0.06	1.32	2.24	6.63	*pacificus*	−7
LOME Pulse 1	1.84–1.86	1.85	Calcareous shale	0.09	2	3.39	6.87	*pacificus*	−7
Background	1.82–1.84	1.83	shale	0.04	0.62	–	8.36	*pacificus*	
Background	1.79–1.81	1.8	shale	0.04	0.56	–	7.98	*pacificus*	
	1.76–1.79	1.775	shale	0.1	2.41	4.09	6.29	*pacificus*	
	1.73–1.76	1.745	shale	0.1	1.68	2.85	5.49	*pacificus*	
	1.69–1.73	1.71	shale	0.09	2.11	3.58	2.73	*pacificus*	
LOME Pulse 2	Average	2.375	Limestone	0.42	7.4	12.54	0.37	*extraordinarius*	+7
	SD			0.19	1.65	2.79	0.26		
LOME Pulse 1	Average	1.875	Calcareous shale	0.07	1.56	2.65	6.16	*pacificus*	−7
	SD			0.02	0.31	0.53	0.84		
Background	Average	1.815	shale	0.04	0.59	–	8.17	*pacificus*	
	SD			0	0.03	–	0.19		

Table 2. Coronene index data from the Wangjiawan River section, South China. SST records are based on Finnegan et al.[4]. Total organic carbon (TOC) data from Jones et al.[21]. See Table S1 for coronene data in the other mass extinctions. SD: standard deviation.

Extinction (eTE) fall within the same medium range and are not significantly different from the background, as supported by a P value of 0.38, which exceeds the significance threshold of 0.05.

Discussion

Late ordovician mass extinction and its causes

The causes of major mass extinctions, apart from the LOME, have been primarily linked to extreme heating events, such as Large Igneous Province (LIP) eruptions or asteroid impacts[10,12]. In the following three subsections, I discuss the primary drivers of the LOME.

LOME first pulse: Cooling and glaciation

The first pulse of the LOME coincided with a transition to shallower facies, where limestone interbedded with dark gray shale at Wangjiawan indicates a shallowing event[21]. This event aligns with the onset of the Hirnantian glaciation, which lasted approximately 0.5 million years at 443 Ma, as evidenced by U-Pb ages of 444.65 ± 0.22 Ma (middle *Dicellograptus complexus* Biozone), 444.06 ± 0.20 Ma (lower *Paraorthograptus pacificus* Biozone), 443.81 ± 0.24 Ma (upper *Tangyagraptus typicus* Subzone), and 442.99 ± 0.17 Ma (upper *Metabolograptus extraordinarius* Biozone)[30]. This strongly supports a link between LOME Pulse 1 and global cooling. Further evidence of cooling from the upper *Paraorthograptus pacificus* zone to the *Metabolograptus extraordinarius* zone is provided by the Chemical Index of Alteration (CIA)[32].

LOME second pulse: Volcanic influence and environmental stress

The second pulse of the LOME corresponds to the termination of the Hirnantian glaciation[21]. This study likely provides the first record of polycyclic aromatic hydrocarbons (PAHs), including coronene, spanning the LOME.

Mercury-to-total organic carbon (Hg/TOC) spikes associated with both pulses of the LOME have been reported across multiple locations[33–37], indicating a global volcanic influence. While some studies[33,38] have argued that Δ^{199}Hg data show no definitive evidence of volcanic influence, Δ^{199}Hg and δ^{202}Hg alone cannot entirely exclude volcanic contributions during the Hirnantian. In contrast, Hu et al.[38] suggested that major volcanic eruptions played a role in the LOME based on Hg isotope data. Multiple K-bentonite layers in South China, attributed to continental margin arc volcanism, are considered a product of volcanic activity that occurred during global cooling[30].

Elevated values of the EGC index and Hg/TOC[21] were recorded during LOME Pulse 1 and Pulse 2 at Wangjiawan, whereas background samples showed no such enrichment (Table S1). These patterns indicate that the 5- to 7-ring PAHs and Hg were likely sourced from volcanic activity.

Declining seawater $^{87}Sr/^{86}Sr$ ratios from the Middle to Late Ordovician have been attributed to increased volcanic activity[39] or a potential superplume event[40]. This could be linked to the emplacement of a now-eroded basaltic trap on a continental landmass. Furthermore, mass-independent sulfur isotope fractionation during the

LOME suggests a stratospheric volcanic eruption, which may have caused severe environmental disruptions[41]. Sial et al.[37] reported Δ^{199}Hg values close to 0‰ for LOME Pulse 2, supporting the presence of volcanic Hg emissions.

Volcanism as a key driver of the LOME

Intense volcanism during the middle-to-late Katian was closely linked to a rapid decline in biodiversity. Prolonged volcanic activity (spanning 3–4 million years) likely imposed sustained ecological stress, ultimately triggering the first pulse of the LOME. Additionally, a major volcanic episode at the Hirnantian–Rhuddanian boundary coincided with the second pulse of the LOME. This temporal alignment supports a volcanic driver for the biotic crisis[42].

A newly identified LIP in northern Iran, extending approximately 1,700 km in length, 100–700 km in width, and over 1,000 km in thickness, peaked during the late Katian–Hirnantian and Silurian periods. This LIP is a strong candidate for the primary driver of the climatic and environmental disruptions that led to the LOME[43]. Furthermore, volcanic ash layers in South China and Europe during the Ordovician–Silurian (O–S) transition suggest that intense volcanism closely coincided with both extinction pulses, further supporting volcanism as a major stressor contributing to the LOME[44].

Geochemical evidence for ten crises in the main mass extinctions

Geochemical evidence supports the presence of multiple extinction pulses. The first and second pulses of the LOME are characterized by Hg/TOC and EGC anomalies, with a notable coronene anomaly exclusively observed in the second pulse[10,21,45].

The Frasnian-Famennian mass extinction event is marked by Hg or Hg/TOC anomalies[15,46–50] and a coronene (7-ring PAH) anomaly[15]. Another Hg/TOC spike in the *triangularis* zone of the early Famennian[15,46,47,50] coincides with a coronene spike[15].

Both the EPE and the eTE exhibit Hg and Hg/TOC anomalies[14,51–53], along with coronene anomalies[14].

The initial phase of the ETME is associated with Ir (ppt level), Hg, and Hg/TOC anomalies, as well as a benzo[ghi]perylene (six-ring PAH) anomaly. This was followed by post-extinction warming, indicated by additional Hg and Hg/TOC anomalies[16,54–56] and a coronene anomaly[16,57].

The KPgME is characterized by Ir (ppb level)[58], Hg, and Hg/TOC anomalies in ocean surface waters[59,60], along with a coronene anomaly[19,61]. A delayed extinction phase, affecting deep-dwelling fauna, is marked by moderate coronene enrichment[19].

Notes on climate changes

The duration between paired extinction events in major mass extinctions ranges from 0.06 to 0.5 million years. The shortest intervals (0.06–0.1 million years) occurred during the PTME and KPgME, likely due to brief periods of global cooling followed by global warming. In contrast, the other three major mass extinctions were primarily linked to large-scale volcanic activity, leading to prolonged cooling phases that lasted for 0.2 to 0.5 million years during eruptions.

A cooling maximum occurred during Event 2 of the ETME due to the continuous supply of SO_2 from sill contact metamorphism and eruptions in the Central Atlantic Magmatic Province (CAMP). This cooling took place under low atmospheric CO_2 levels and was later followed by warming as CO_2 concentrations increased[62,63], coinciding with a transition from sill volcanism to magma volcanism in Event 3[16]. As a model calculation example for ETME, global mean surface temperatures dropped by approximately 8 °C due to frequent injections of SO_2 and CO_2 (125 GtS and ~ 5300 GtC) over a period of 1,200 years[64].

Evidence from cuticle surface morphology and leaf-shape SO_2 proxies near the Triassic–Jurassic (T–J) boundary in Greenland indicates elevated SO_2 concentrations in the troposphere[63,65]. These proxies suggest a significant injection of SO_2 into the atmosphere just below the onset of the initial carbon isotope excursion (CIE) leading into the main CIE[62]. This initial SO_2 enrichment coincided with both plant turnover and marine extinction events.

Climate uncertainty during the end-Permian extinction

Recent studies have shown that terrestrial extinction during the EPE occurred diachronously across latitudes, beginning at high latitudes during the late Changhsingian and progressing toward the tropics by the early Induan[66,67]. This pattern has been interpreted as the result of a latitudinal gradient of environmental stressors—ranging from extreme warming at high latitudes to compounded thermal pressures at lower latitudes—that collectively fueled ecosystem collapse. Additionally, mega El Niño events may have intensified climate variability and mean state warming, ultimately leading to catastrophic but temporally staggered terrestrial and marine extinctions associated with the Permian-Triassic mass extinction (PTME)[68].

However, the EPE presents a significant unresolved climate anomaly. Notably, no substantial change in surface temperature has been detected during the main extinction phase of the EPE[7], as evidenced by sedimentary records from a 2 cm thick layer located between 4 and 2 cm below the top of Bed 24e in Meishan section A[69]. This observation is further supported by the extinction horizon at the top of Bed 24e, described by Song et al.[23], which occurs prior to the warming phase recorded in Bed 26 of the same section[7]. These findings highlight ongoing uncertainty regarding short-term climate fluctuations during the critical extinction interval of the EPE.

During the EPE, explosive eruptions of the Siberian Traps released large volumes of stratospheric SO_2, which contributed to the formation of sulfuric acid aerosols. Evidence for this includes Hg/TOC ratios, coronene index, and coronene/phenanthrene anomalies[14,52,53], along with the coincident ages of pyroclastic rocks and sills in the Siberian Large Igneous Province (LIP)[26]. The deposition of pyroclastic material during these eruptions is temporally associated with the PTME suggesting a direct causal link between volcanic activity and subsequent

climatic and ecological disruption[14]. These aerosols, once dispersed in the stratosphere, would have reflected sunlight, leading to reduced solar radiation and short-term global cooling.

However, such brief cooling events are difficult to detect using conventional temperature proxies due to their short duration and poor preservation in the geologic record. Nonetheless, the diachronous pattern of terrestrial extinction, starting at high latitudes during the late Changhsingian and migrating toward the tropics by the early Induan, supports a scenario of initial global cooling followed by global warming.

Gas production temperature and climate change

The relationship between coronene index values and gas production temperature has been analyzed using heating experimental data on PAHs from Norinaga et al.[18], Kaiho et al.[16], and Kaiho[12]. This correlation suggests that the classification of mass extinctions based on coronene index values and global surface temperature anomalies is linked to the heating temperatures and durations required for gas and soot production[12].

The results of this study indicate that coronene index values correspond to global surface temperature anomalies during ten extinction events across the five major mass extinctions, as detailed in the results section. Low-temperature heating of sulfides and high-temperature heating of sulfates and organic matter lead to the release of SO_2 and soot, respectively, both of which drive global cooling (Fig. 1). High-temperature heating also causes CO_2 emissions; however, this process initially results in cooling, followed by subsequent warming[19,70,71]. In contrast, intermediate-temperature heating of hydrocarbons and carbonates results in CO_2 emissions, triggering global warming after an initial cooling phase induced by SO_2 from sulfides.

Notably, heating temperatures transitioned from low to medium during the LOME and the ETME, while they shifted from high to medium during the FFME and the KPgME, influencing climate changes (Fig. 1). This mechanism explains the recurring pattern of cooling-driven mass extinctions followed by warming phases, which can also contribute to delayed extinction events. Importantly, all five major mass extinctions concluded during a period of global warming, which was preceded by global cooling.

Mechanism of climate change corresponding to Coronene index values

The concentrations of SO_2 in the stratosphere and CO_2 in the atmosphere during volcanic-driven extinction events were critical factors influencing climate change[12]. Both gases were released through the thermal metamorphism of sedimentary rocks in Large Igneous Provinces (LIPs)[12,16,72]. Additionally, mercury (Hg) was mobilized from aureoles formed by sill contact metamorphism[73]. Hg release from these aureoles begins at temperatures of approximately 265–300 °C, lower than the temperatures required for SO_2 and CO_2 formation. This suggests that all volcanic events released Hg, though its release mechanism differed from that of SO_2 and CO_2 due to variations in temperature conditions, volcanic processes, and the depth of affected sedimentary rocks (Fig. 1). Notably, Hg/TOC spikes closely corresponded with coronene index spikes—or (e + ghi + cor)/phe peaks—during the FFME, PTME, and ETME[14–16].

A significant portion of organic-rich sedimentary rocks in the Siberian Traps was intruded by sills, coinciding with the PTME[71]. Vitrinite index and *Tmax* data from Svensen et al.[74] suggest that PAHs could not have survived within high-temperature aureoles. However, PAH formation was possible in zones near the aureoles, though some may have been lost due to prolonged heating. Thermal modeling suggests that these rocks released substantial amounts of both organic and inorganic CO_2 during sill contact metamorphism[74]. At the end of the Permian, estimated CO_2 emissions from Siberian Traps sill contact metamorphism were approximately 100,000 Gt CO_2, based on data from Svensen et al.[74]. This accounts for about 55% (ranging from 30 to 160%) of the estimated mantle-derived CO_2 emissions from the Siberian Traps, which averaged 192,000 Gt CO_2 (range: 64,000–320,000 Gt CO_2)[71]. These findings suggest that the volume of gases generated from the thermal metamorphism of sedimentary rocks was comparable to—or even greater than—that produced by volcanic eruptions alone.

Heating temperature transitions and volcanic style changes

The transition in heating temperature may have been driven by a shift in volcanic style—from sill contact metamorphism to magmatic eruptions—during the PTME and ETME. In the case of the Cretaceous-Paleogene Mass Extinction (KPgME), an asteroid impact was followed by CO_2 emissions, either from the impact itself[19] or from subsequent Deccan Traps volcanism. For the FFME, deep sill contact metamorphism may have preceded magmatic eruptions due to the presence of sedimentary rock layers that were nearly twice as thick as those associated with the other four mass extinctions. The temperature range of 400–600 °C, sustained over approximately 100 years in aureoles, is consistent with the degassing temperatures required for SO_2 and CO_2 release (Fig. 1). Based on heating temperature variations, the LOME is grouped with the PTME and ETME, where volcanic activity transitioned from sill contact metamorphism to magmatic eruptions[16].

SO_2 and CO_2 originated from sedimentary rock aureoles, magma eruptions, and meteorite impacts, while PAHs and black carbon likely derived specifically from magma eruptions and impact events. The heating of sedimentary rocks by volcanic activity and asteroid impacts played a critical role in climate change during mass extinctions. This process typically began with global cooling, associated with the initial extinction phase, followed by global warming, which contributed to delayed extinctions or crisis phases. These temperature transitions were driven by variations in heating intensity, which depended on the depth and proximity of sedimentary rocks to magma in the first four major mass extinctions[12]. However, the KPgME differed due to the primary influence of the asteroid impact or the combined effects of the impact and subsequent volcanism. Evidence supporting this includes high Hg/TOC values in the K-Pg boundary red layer[59].

This pattern suggests that volcanism was the primary driver of four major mass extinctions, while the KPgME was uniquely triggered by an impact event. Evidence of sedimentary rock heating during these events is summarized in Table 3. The presence of sills in LIPs, along with thick sedimentary rock deposits (3–4 km for the PTME, 3–5 km for the ETME, and 6–8 km for the FFME), as well as the ~ 3 km-thick sedimentary layers at the

Mass extinction	Age of extinction (Ma)	Location of heating	Age of heating (Ma)	Evidence of heating	Presence of sill	Thickness of sedimentary rock (km)
K-Pg	66.0	Chicxulub[19], DT[10]	66.0	Impact crater, LIP	Yes	3 for impact
end-Triassic	201.56	CAMP[16]	201.6–201.0	Sill	Yes	3–4
P-T	251.9	Siberian Trap[72–74]	251.9	Pyroclastic, sill	Yes	3–5
F-F	371.9	Yakutsk-Viluy LIP[47]	374 ± 3.5	Eruption	Yes	7–8
		PDD LIP[47]	377–370	Rift structure	Yes	6–6.5
Late Ordovician	443	Northern Iran LIP[43]	451–443	Basaltic lava, rhyolite, sill	Minor?	2–4[84]

Table 3. Evidence of heating of sedimentary rocks in each major mass extinction. DT: Deccan Traps. CAMP: Central Magnetic Province. PDD: Pripyat-Dnieper-Donets. LIP: Large Igneous Province. See also Kaiho[12] for related references.

		Long-term trend	Long-term cycle (> 1 m.y.)	Short-term event (< 0.1 m.y.)			
Event	Event age (Gyr)	Long-term temperature (°C)	Long-term temperature + climate cycle (°C)	Temp. anomaly cooling event (°C)	Temp. during cooling event (°C)	Temp. anomaly aftermath warming (°C)	Temp. during warming event (°C)
-1	−0.066	13	22	−12	10	+7	29
−2	−0.201	12	22	−8	14	+7	29
−3	−0.252	12	22	?	?	+14	36
−4	−0.372	10	19	−8	11	+11	30
−5	−0.444	10	18	−10	8	+10	28

Table 4. Earth's average surface temperature based on long-term trends, long-term climate cycles, and short-term events with associated temperature anomalies during major mass extinction events. Long-term temperature data are from Mello and Friaça[85]; long-term climate cycle data are from Scotese et al.[86]; temperature anomaly data are from Kaiho[27].

Chicxulub impact site, further supports the hypothesis that sedimentary rock heating significantly contributed to the environmental disruptions associated with mass extinctions[12].

Thermal forcing in mass extinctions

Magmatic intrusions, including sills, heat sedimentary rocks and release SO_2 and CO_2 over timescales of approximately 100 years. Once in the stratosphere, SO_2 is converted into sulfuric acid aerosols, which reflect sunlight and trigger global cooling. Similarly, meteorite impacts heat sedimentary target rocks, generating soot in the short term. This soot forms aerosols that disperse globally, absorbing sunlight and inducing global cooling as well[19].

The coronene index has been applied to investigate both the initial and delayed extinction phases across the five major mass extinction events. The initial extinction phases, such as those during the Late Ordovician and end-Triassic, were associated with low-temperature heating. In contrast, the FFME and KPgME were linked to high-temperature heating, which produced SO_2 and soot, contributing to severe global cooling.

All delayed marine extinction or crisis phases during these five events were associated with intermediate-temperature heating, primarily releasing CO_2 and driving subsequent global warming. Overall, mass extinction events typically involved two stages: an initial global cooling phase followed by a warming phase. These were driven by volcanic or impact-related heating and emissions of SO_2, SO_3, soot, and CO_2. The observed transitions in heating temperature may reflect changes in volcanic activity, shifting from sill-induced degassing to magma eruptions, or transitions from meteorite impacts to post-impact volcanism.

Most terrestrial and marine metazoans can survive within a temperature range of 10–40 °C[75,76]. Global cooling during the first stage of mass extinctions is estimated to have caused a ~ 10 °C drop in average global surface temperature, aligning with the modern annual average temperature at approximately 37° N latitude oceanic climates. This suggests that metazoans inhabiting regions between 37° and 90° latitude would have faced extinction as survival thresholds based on annual average temperatures (which account for even colder winters) were exceeded. Consequently, these cooling phases primarily triggered extinctions in high and mid-latitude regions, driven mainly by declining surface temperatures.

Conversely, global warming during the second stage of mass extinctions likely pushed average global surface temperatures to ~ 30 °C or higher—except during the EPE, which reached ~ 36 °C. At the EPE, such extreme temperatures would have exceeded the thermal tolerance of low-latitude metazoans, causing widespread tropical extinctions, in contrast to other events where extreme warming did not fully manifest except as deep-water anoxia.

This two-phase model aligns with observed patterns of extinction severity: high extinction rates during the initial cooling phase, and comparatively lower rates during the subsequent warming phases of the FFME, ETME, and KPgME, as these later events involved only minor warming during the delayed extinction phases.

Moreover, the pattern of terrestrial extinctions progressing from high latitudes before the EPE, to middle latitudes around the EPE, and low latitudes around the eTE, as documented by Wu et al.[66] and Zhang et al.[67], is also consistent with my theory of a two-stage "cooling-warming" extinction mechanism.

Methods

Geological setting and samples

The Wangjiawan section, which spans the Ordovician–Silurian transition, is located in the South China Craton (30° 58' 56"N, 111° 25' 10"E for the Wangjiawan North section.)[77]. In ascending stratigraphic order, the Wufeng, Kuanyinchiao, and Lungamachi Formations cover the uppermost Ordovician and lower Silurian periods. The Wufeng and Lungamachi Formations consist of dark shales with occasional chert, containing abundant graptolite fossils[78,79]. The Kuanyinchiao Formation is a thin (less than 50 cm thick) argillaceous limestone containing numerous shelly fossils, including the Hirnantian fauna[78].

The Kuanyinchiao Formation marks a significant drop in eustatic sea level[80], and the associated Hirnantian fauna are recognized as cool or cold-water species[78]. This event corresponds to global cooling and the sequestration of water into the Gondwanan ice caps during the Hirnantian glacial episode. Two extinction episodes, named the 1 st phase of LOME and the 2nd phase of LOME, occurred at the beginning and end of the Hirnantian glacial episode, respectively[21,78,79].

The Wangjiawan (River) section is located in the Wangjiawan River, near the southeastern end of Wangjiawan village, approximately 42 km north of Yichang city. The Wangjiawan (River) section, located about 10 m south of the Riverside section (about 280 m south of the Wangjiawan North section), represents the Hirnantian (Late Ordovician) interval. The River section is less weathered than the Riverside section, making it more suitable for geochemical analysis. I collected continuous shale and limestone samples from the River section[21].

Samples from three sections (Coumiac [GSSP], Sinsin, and Yangdi) in France, Belgium, and China spanning the F-F boundary[15], three sections (Meishan [GSSP], Liangfengya [LFY], and Bulla) in China and Italy spanning the end-P mass extinction[14], and two sections (Kuhjoch [GSSP], St. Audrie's Bay) spanning the end-T mass extinction[16] consist of limestones, marls, and shales deposited on continental shelves. The K-Pg boundary samples include dark gray clay deposited at depths of 200 to 1000 m from Caravaca, Spain[81,82], and impact turbidites and marl deposited in the deep sea at Beloc, Haiti[19,83].

PAH analyses

Fourteen samples collected from intervals near two extinction events were analyzed for polyaromatic hydrocarbons (PAHs). Approximately 120 g of each sample was powdered after removing surface contaminants by cutting and washing with dichloromethane/methanol (6:4, v/v). The powdered samples (100 g) were then Soxhlet-extracted with dichloromethane/methanol (7:1, v/v) for 48 h. The extracts were dried over Na_2SO_4 and concentrated by evaporation under reduced pressure.

The concentrated extracts were separated into four fractions (F1a, F1b, F2, F3–8) on a silica gel column (0.6 g of silica, 63–200 μm) using the following solvents: 2 ml of *n*-hexane (F1a), 4 ml of *n*-hexane (F1b), 3 ml of n-hexane/toluene (3:1 v/v) (F2), and 1 ml of ethyl acetate and 10 ml of methanol (F3–8).

The aromatic hydrocarbon fractions (combinations of F1b and F2) from each extraction were analyzed using gas chromatography–mass spectrometry (GC-MS). Organic compounds were identified using an Agilent 7890B gas chromatograph interfaced with an Agilent 7000 triple quadrupole mass spectrometer, operated with an ionizing electron energy of 70 eV and scanned from m/z 50 to 600 with a scan time of 0.34 s. A fused silica HP-5MS capillary column (length: 30 m, internal diameter: 0.25 mm, film thickness: 0.25 μm) was used, with helium as the carrier gas. Samples were injected at 50 °C, held at this temperature for 1 min, then the temperature was raised to 120 °C at a rate of 30 °C/min, followed by an increase to 310 °C at a rate of 5 °C/min, and then held at 310 °C for 20 min.

The analyzed samples show no evidence of organic molecule contamination, as confirmed by the Rc (MPR) index[14–16,19]. The Wangjiawan samples contained sufficient amounts of PAHs but only trace amounts of *n*-alkanes, hopanes, and steranes for the analyses, supporting the absence of contamination. Complete datasets from continuous sampling at the River section will be published in a forthcoming study. Importantly, biomarker concentrations were measured well above detection limits and blank sample values, ensuring the reliability of the results. GC-MS chromatograms in Fig. 6 of Kaiho et al. (2022), Figure A1 of Kaiho et al. (2021), Figure DR1 of Kaiho et al. (2020), and Figure S1 show that the peaks of phenanthrene, benzo(e)pyrene, benzo(ghi) perylene, and coronene are completely separated and well-resolved. The blank control values are 0.007 ng/g for phenanthrene and below the detection limit (0.000 ng/g) for benzo(e)pyrene, benzo(ghi)perylene, and coronene, which are much lower than the concentrations found in the studied rock samples.

Coronene index

The coronene index, a proxy for sedimentary rock heating temperature, is defined as: coronene/(benzo(e) pyrene + benzo(ghi)perylene + coronene)[14]. This definition reflects the relative formation temperatures of these compounds, with coronene having the highest formation temperature, benzo(ghi)perylene the second highest, and benzo(e)pyrene the lowest among the 5–7 ring polycyclic aromatic hydrocarbons (PAHs)[14,18]. The correlation between coronene index values and gas production temperatures has been established using heating experimental data on PAHs from Norinaga et al.[18], Kaiho et al.[16], and Kaiho[12] (Fig. 1).

EGC index

The EGC index, a proxy for heating events such as large-scale volcanism and asteroid impacts, is calculated as the sum of representative 5- to 7-ring PAHs—benzo(e)pyrene, benzo(ghi)perylene, and coronene—standardized by

the 3-ring PAH phenanthrene, making it applicable to a wide range of low to high-temperature conditions[14,18]. This index is further supported by experimental heating data on PAHs from Norinaga et al.[18] (Fig. 1).

T test

T tests for both the coronene index and EGC index were performed to assess differences between each extinction event and background levels.

Calculation of global surface temperature

Surface temperature anomalies at low latitudes consistently exhibit intermediate values, indicating proximity to average values[27]. The error margin for SST anomalies in geological ages is approximately 1 °C[27]. SST anomalies from various geological ages[4–9] were converted to global surface temperature anomalies and land-surface temperature anomalies using Fig. 1d of Kaiho[27], which was generated from global cooling and warming (recovery) data obtained through climate model calculations[67]. These data are presented in Table S1.

Data availability

Data is provided within the manuscript or supplementary information files.

Received: 14 February 2025; Accepted: 5 May 2025
Published online: 12 May 2025

References

1. Sepkoski, J. J. Jr. Patterns of Phanerozoic extinctions: A perspective from global data bases, in *Global Event Stratigraphy* (ed. Walliser, O. H.) 35–52 (Berlin, Heidelberg, Germany, Springer-Verlag, (1996).
2. Bambach, R. K. Phanerozoic biodiversity mass extinctions. *Ann. Rev. Earth Planet. Sci.* **34**, 127–155 (2006).
3. Benton, M. J. The origins of modern biodiversity on land. *Phil Trans. R Soc. B*. **365**, 3667–3679 (2010).
4. Finnegan, S. et al. The magnitude and duration of late Ordovician–Early silurian glaciation. *Science* **331**, 903–906 (2011).
5. Balter, V., Renaud, S., Girard, C. & Joachimski, M. M. Record of climate-driven morphological changes in 376 ma devonian fossils. *Geology* **36**, 907–910 (2008).
6. Huang, C., Joachimski, M. M. & Gong, Y. Did climate changes trigger the late devonian Kellwasser crisis?? Evidence from a high-resolution conodont $\delta^{18}O_{PO4}$ record from South China. *Earth Planet. Sci. Lett.* **495**, 174–184 (2018).
7. Chen, J. et al. High-resolution SIMS oxygen isotope analysis on conodont apatite from South China and implications for the end-Permian mass extinction. *Palaeogeogr Palaeoclimatol Palaeoecol.* **448**, 26–38 (2016).
8. Korte, C., Hesselbo, S. P., Jenkyns, H. C., Rockaby, R. E. & Spoetl, C. Palaeoenvironmental significance of carbon- and oxygen-isotope stratigraphy of marine Triassic–Jurassic boundary sections in SW Britain. *J. Geol. Soc. Lond.* **166**, 431–445 (2009).
9. Vellekoop, J. et al. Rapid short-term cooling following the Chicxulub impact at the Cretaceous-Paleogene boundary. *Proc. Nat. Acad. Sci. USA*. **111**, 7537–7541 (2014).
10. Bond, D. P. G. & Grasby, S. On the causes of mass extinctions. *Palaeogeogr Palaeoclimatol Palaeoecol.* **478**, 3–29 (2017).
11. Rampino, M. R., Caldeira, K. & Rodriguez, S. Sixteen mass extinctions of the past 541 my correlated with 15 pulses of large igneous Province (LIP) volcanism and the 4 largest extraterrestrial impacts. *Glob Planet. Chang.* **234**, 104369 (2024).
12. Kaiho, K. Role of volcanism and impact heating in mass extinction climate shifts. *Sci. Rep.* **14** https://doi.org/10.1038/s41598-024-60467-y (2024).
13. Qiu et al. A nutrient control on expanded anoxia and global cooling during the late ordovician mass extinction. *Comm. Earth Environ.* **3**, 82 (2022).
14. Kaiho, K., Aftabuzzaman, M., Jones, D. S. & Tian, L. Pulsed volcanic combustion events coincident with the end-Permian terrestrial disturbance and the following global crisis. *Geology* **49**, 289–293 (2020).
15. Kaiho, K. et al. Coronene, Mercury, and biomarker data support a link between extinction magnitude and volcanic intensity in the late devonian. *Glob Planet. Chang.* **199**, 103452 (2021).
16. Kaiho, K. et al. Volcanic temperature changes modulated volatile release and climate fluctuations at the end-Triassic mass extinction. *Earth Planet. Sci. Lett.* **579**, 117364 (2022).
17. Saito, R., Kaiho, K., Tian, L. & Takahashi, S. Frequent high-temperature volcanic combustion events delayed biotic recovery after the end-Permian mass extinction. *Earth Planet. Sci. Lett.* **614**, 118194 (2023).
18. Norinaga, K., Deutschmann, O., Saegusa, N. & Hayashi, J. I. Analysis of pyrolysis products from light hydrocarbons and kinetic modeling for growth of polycyclic aromatic hydrocarbons with detailed chemistry. *J. Anal. Appl. Pyrol.* **86**, 148–160 (2009).
19. Kaiho, K. et al. Global climate change driven by soot at the K–Pg boundary as the cause of the mass extinction. *Sci. Rep.* **6**, 28427. https://doi.org/10.1038/srep28427 (2016).
20. Chen, J., Walter, M. R., Logan, G. A., Hinman, M. C. & Summons, R. E. The paleoproterozoic mcarthur river (HYC) Pb/Zn/Ag deposit of Northern Australia: organic geochemistry and ore genesis. *Ear Planet. Sci. Lett.* **210**, 467–479 (2003).
21. Jones, D. S., Martini, A. M., Fike, D. A. & Kaiho, K. A volcanic trigger for the late ordovician mass extinction? Mercury data from South China and Laurentia. *Geology* **45**, 631–634 (2017).
22. Bond, D. P. G. & Grasby, S. Late ordovician mass extinction caused by volcanism, warming, and anoxia, not cooling and glaciation. *Geology* **48**, 777–781 (2020).
23. Song, H., Wignall, P. B., Tong, J. N. & Yin, H. F. Two pulses of extinction during the Permian-Triassic crisis. *Nat. Geosci.* **6**, 52–56 (2013).
24. Fox, C. P., Cui, X., Whiteside, J. H., Olsen, P. E. & Summons, R. E. Molecular and isotopic evidence reveals the end-Triassic carbon isotope excursion is not from massive exogenous light carbon. *Proc. Nat. Acad. Sci., USA* 117, 30171–30178 (2020).
25. Gradstein, F. M., Ogg, J. G., Schmitz, M. D. & Ogg, G. M. *Geologic Time Scale.* Vol 1Elsevier,. (2020).
26. Burgess, S. D., Muirhead, J. D. & Bowring, S. A. Initial pulse of Siberian traps sills as the trigger of the end-Permian mass extinction. *Nat. Commun.* **8**, 164. https://doi.org/10.1038/s41467-017-00083-9 (2017).
27. Kaiho, K. Relationship between extinction magnitude and climate change during major marine and terrestrial animal crises. *Biogeosci* **19**, 3369–3380 (2022).
28. Vellekoop, J. et al. Evidence for Cretaceous-Paleogene boundary bolide impact winter conditions from new Jersey, USA. *Geology* **44**, 619–622 (2016).
29. Trotter, J. A. et al. Did cooling oceans trigger ordovician biodiversification? Evidence from conodont thermometry. *Science* **321**, 550–554 (2008).
30. Ling, M. et al. An extremely brief end ordovician mass extinction linked to abrupt onset of glaciation. *Solid Earth Sci.* **4**, 190–198 (2019).
31. Liao, R. & Sun, W. Late ordovician mass extinction caused by global warming or cooling? *Acta Geochim.* **39**, 595–598 (2020).

32. Lin, D., Tang, S., Xi, Z., Zhang, B. & Ye, Y. Geochemical Characteristics of Late Ordovician Shales in the Upper Yangtze Platform, South China: Implications for Redox Environmental Evolution. *Minerals* 11, 710 (2021). (2021).
33. Shen, J. et al. Mercury in marine ordovician/silurian boundary sections of South China is sulfide-hosted and non-volcanic in origin. *Earth Planet. Sci. Lett.* **511**, 130–140 (2019).
34. Lu, Y. et al. Seawater sources of hg enrichment in Ordovician-Silurian boundary strata, South China. *Palaeogeogr Palaeoclimatol Palaeoecol*. **601**, 111156 (2022).
35. Wang et al. The influence of late ordovician volcanism on the marine environment based on high-resolution mercury data from South China. *GSA Bull.* **135**, 787–798 (2023).
36. Liu, Y. et al. Terrestrial rather than volcanic mercury inputs to the Yangtze platform (South China) during the Ordovician-Silurian transition. *Glob Planet. Chang.* **220**, 104023 (2023).
37. Sial et al. Hg isotopes and elemental chemostratigraphy across the Ordovician–Silurian transition in the Argentine precordillera: implications for the link between volcanism and extinctions. *Gondwana Res.* **133**, 270–296 (2024).
38. Hu, D. et al. Major volcanic eruptions linked to the late ordovician mass extinction: evidence from mercury enrichment and hg isotopes. *Glob Planet. Chang.* **196**, 103374 (2021).
39. Young, S. A. et al. A major drop in seawater $^{87}Sr/^{86}Sr$ during the Middle Ordovician (Darriwilian): links to volcanism and climate? *Geology* 37, 951–954 (2009).
40. Lefebvre, V., Servais, T., Franc¸ois, L. & Averbuch, O. Did A Katian large igneous Province trigger the late ordovician glaciation? A hypothesis tested with A carbon cycle model. *Palaeogeogr Palaeoclimatol Palaeoecol.* **296**, 310–319 (2010).
41. Hu, D. et al. Large mass-independent sulphur isotope anomalies link stratospheric volcanism to the late ordovician mass extinction. *Nat. Commun.* **11** https://doi.org/10.1038/s41467-020-16228-2 (2020).
42. Yang, S., Hu, W., Fan, J. & Deng, Y. New geochemical identification fingerprints of volcanism during the Ordovician-Silurian transition and its implications for biological and environmental evolution. *Earth-Sci. Rev.* **228**, 104016 (2022).
43. Drakhshi, M., Ernst, R. E. & Kamo, S. L. Ordovician-Silurian volcanism in Northern Iran: implications for a new large igneous Province (LIP) and a robust candidate for the late ordovician mass extinction. *Gondwana Res.* **107**, 256–280 (2022).
44. Yang, S. et al. Duration, evolution, and implications of volcanic activity across the Ordovician–Silurian transition in the lower Yangtze region, South China. *Earth Planet. Sci. Lett.* **518**, 13–25 (2019).
45. Jia, J., Du, X. & Ma, Z. Different integrated mechanisms drove the two pulses of the late ordovician mass extinction. *Palaeogeogr Palaeoclimatol Palaeoecol*. **620**, 111572 (2023).
46. Racki, G., Rakociński, M., Marynowski, L. & Wignall, P. B. Mercury enrichments and the Frasnian-Famennian biotic crisis: A volcanic trigger proved? *Geology* **46**, 543–546 (2018).
47. Racki, G. A volcanic scenario for the Frasnian-Famennian major biotic crisis and other late devonian global changes: more answers than questions? *Glob Planet. Chang.* **189**, 103174 (2020).
48. Liu et al. Upper devonian mercury record from North America and its implications for the Frasnian–Famennian mass extinction. *Palaeogeogr Palaeoclimatol Palaeoecol*. **576**, 110502 (2021).
49. Zhang et al. Mercury anomalies link to extensive volcanism across the late devonian Frasnian–Famennian boundary in South China. *Front. Earth Sci.* **9**, 691827 (2021).
50. Zhao et al. Mercury isotope evidence for regional volcanism during the Frasnian-Famennian transition. *Earth Planet. Sci. Lett.* **581**, 117412 (2022).
51. Grasby, S. E. et al. Isotopic signatures of mercury contamination in latest permian oceans. *Geology* **45**, 55–58 (2017).
52. Wang, X. D. et al. Mercury anomalies across the end permian mass extinction in South China from shallow and deep water depositional environments. *Earth Planet. Sci. Lett.* **496**, 159–167 (2018).
53. Shen, J. et al. Evidence for a prolonged Permian-Triassic extinction interval from global marine mercury records. *Nat. Commun.* **10** https://doi.org/10.1038/s41467-019-09620-0 (2019).
54. Tanner, L. H., Kyte, F. T., Richoz, S. & Krystyn, L. Stratigraphic distribution of iridium across the Triassic-Jurassic boundary in the GSSP section at Kuhjoch, Austria. *Palaeogeogr Palaeoclimatol Palaeoecol*. **449**, 13–26 (2016).
55. Percival, L. M. E. et al. Mercury evidence for pulsed volcanism during the end-Triassic mass extinction. *Proc. Nat. Acad. Sci.* 114, 7929–7934 (2017).
56. Lindström, S. et al. Tracing volcanic emissions from the central Atlantic magmatic Province in the sedimentary record. *Earth Sci. Rev.* **212**, 103444 (2021).
57. Fox, C. P., Whiteside, J. H. & Grice, K. Flame out! End-Triassic mass extinction polycyclic aromatic hydrocarbons reflect more than just fire. *Earth Planet. Sci. Lett.* **584**, 117418 (2022).
58. Alvarez, L. W., Alvarez, W., Asaro, F. & Michel, H. V. Extraterrestrial cause for the Cretaceous-Tertiary extinction. *Science* **208**, 1095–1108 (1980).
59. Sial, A. N. et al. Mercury enrichment and hg isotopes in Cretaceouse–Paleogene boundary successions: links to volcanism and palaeoenvironmental impacts. *Cretac. Res.* **66**, 60e81 (2016).
60. Font, E., Chen, J., Regelous, M., Regelous, A. & Adatte, T. Volcanic origin of the mercury anomalies at the Cretaceous-Paleogene transition of Bidart, France. *Geology* **50**, 142–146 (2022).
61. Arinobu, T., Ishiwatari, R., Kaiho, K. & Lamolda, M. A. Spike of polycyclic aromatic hydrocarbons associated with an abrupt decrease in $\delta^{13}C$ of a terrestrial biomarker at the Cretaceous-Tertiary boundary at Caravaca, Spain. *Geology* **27**, 723–726 (1999).
62. Steinthorsdottir, M., Jeram, A. J. & McElwain, J. C. Extremely elevated CO_2 concentrations at the triassic/jurassic boundary. *Palaeogeogr Palaeoclimatol Palaeoecol*. **308**, 418–432 (2011).
63. Steinthorsdottir, M., Elliott-Kingston, C. & Bacon, K. L. Cuticle surfaces of fossil plants as a potential proxy for volcanic SO_2 emissions: observations from the Triassic–Jurassic transition of East Greenland. *Palaeobio Palaeoenv*. **298**, 49–69 (2018).
64. Landwehrs, J. P., Hofmann, M. & Petri, S. Climatic fluctuations modeled for carbon and sulfur emissions from end-Triassic volcanism. *Earth Planet. Sci. Lett.* **537**, 116174 (2020).
65. Bacon, K. L., Belcher, C. M., Haworth, M. & McElwain, J. C. Increased atmospheric SO_2 detected from changes in leaf physiognomy across the Triassic–Jurassic boundary interval of East Greenland. *PLOS One*. **8**, e60614 (2013).
66. Wu, Q. et al. The terrestrial end-Permian mass extinction in the paleotropics postdates the marine extinction. *Sci. Adv.* **10**, eadi7284 (2024).
67. Zhang, P. et al. Terrestrial mercury anomalies across the Permian-Triassic transition in North China linked to volcanism. *Chem. Geol.* **673**, 122555 (2025).
68. Sun, Y. et al. Mega El Niño instigated the end-Permian mass extinction. *Science* **385**, 1189–1195 (2024).
69. Kaiho, K., Chen, Z. Q., Kawahata, H., Kajiwara, Y. & Sato, H. Close-up of the end-Permian mass extinction horizon recorded in the Meishan section, South China: sedimentary, elemental, and biotic characterization and a negative shift of sulfate sulfur isotope ratio. *Palaeogeogr Palaeoclimatol Palaeoecol*. **239**, 396–405 (2006).
70. Kaiho, K. & Oshima, N. Site of asteroid impact changed the history of life on Earth: the low probability of mass extinction. *Sci. Rep.* **7**, 14855 (2017).
71. Black, B. A. et al. Systemic swings in end-Permian climate from Siberian traps carbon and sulfur outgassing. *Nat. Geosci.* **11**, 949–954 (2018).
72. Svensen, H. et al. Siberian gas venting and the end-Permian environmental crisis. *Earth Planet. Sci. Lett.* **277**, 490–500 (2009).
73. Svensen, H. H., Jones, M. T., Percival, L. M. E., Grasby, S. E. & Mather, T. A. Release of mercury during contact metamorphism of shale: implications for Understanding the impacts of large igneous Province volcanism. *Earth Planet. Sci. Lett.* **619**, 118306 (2023).

74. Svensen, H. H. et al. Sills and gas generation in the Siberian traps. *Phil Trans. R Soc. A*. **376**, 20170080 (2018).
75. Sunday, J. M., Bates, A. E. & Dulvy, N. K. Global analysis of thermal tolerance and latitude in ectotherms. *Proc. R. Soc.*, B 278, 1823–1830 (2011).
76. Araújo, M. B. et al. Heat freezes niche evolution. *Ecol. Lett.* **16**, 1206–1219 (2013).
77. Chen, X., Rong, J. Y., Li, Y. & Boucott, A. J. Facies patterns and geography of the Yangtze region, South China, through the ordovician and silurian transition. *Palaeogeogr Palaeoclimatol Palaeoecol*. **204**, 353–372 (2004).
78. Chen, X. et al. Late ordovician to earliest silurian graptolite and brachiopod biozonation from the Yangtze region, South China, with a global correlation. *Geol. Mag.* **137**, 623–650 (2000).
79. Chen, X. et al. The global stratotype section and point (GSSP) for the base of the Hirnantian stage (the uppermost of the ordovician System). *Episodes* **29**, 183–196 (2006).
80. Fan, J., Peng, P. & Melchin, M. J. Carbon isotopes and event stratigraphy near the Ordovician–Silurian boundary, Yichang, South China. *Palaeogeogr Palaeoclimatol Palaeoecol*. **276**, 160–169 (2009).
81. Coccioni, R. & Galeotti, S. K–T boundary extinction: geologically instantaneous or gradual event? Evidence for deep-sea benthic foraminifera. *Geology* **22**, 779–782 (1994).
82. MacLeod, N. & Keller, G. Comparative biogeographic analysis of planktonic foraminiferal survivorship across the cretaceous/tertiary (K/T) boundary. *Paleobiology* **20**, 143–177 (1994).
83. Keller, G., Adatte, T., Stinnesbeck, W., Stüben, D. & Berner, Z. Age, chemo- and biostratigraphy of Haiti spherule-rich deposits: a multi-event K-T scenario. *Can. J. Earth Sci.* **38**, 197–227 (2001).
84. Ghorbani, M. *Lithostratigraphy of Iran. Springer Geology* (Springer, 2019).
85. Mello, F. S. & Friaça, A. C. The end of life on Earth is not the end of the world: converging to an estimate of life span of the biosphere? *Internat J. Astrobiol.* **19**, 25–42 (2019).
86. Scotese, C. R., Song, H., Mills, B. J. W., Douwe, G. & van der Meer, D. G. Phanerozoic paleotemperatures: the Earth's changing climate during the last 540 million years. *Earth-Sci. Rev.* **215**, 103503 (2021).

Acknowledgements

This work was partially funded by the Japan Society for the Promotion of Science (Grant No. 25247084). I thank Xu Chen for granting access to the study section, Raman K. Biswas for assistance with laboratory work, and Ryosuke Saito for producing Figure 2. I also thank Man Lu and the anonymous referees for their valuable comments.

Authorship contributions

Kunio Kaiho: Conceptualization, Formal analysis, Investigation, Methodology, Writing – original draft, Writing – review & editing.

Declarations

Competing interests

The authors declare no competing interests.

Supplementary Information

Supplementary material related to this article can be found on-line at https://doi.org/10.1038/s41598-025-01203-y.

Additional information

Supplementary Information The online version contains supplementary material available at https://doi.org/10.1038/s41598-025-01203-y.

Correspondence and requests for materials should be addressed to K.K.